

Article

Topology Optimization Design of Multi-Input-Multi-Output Compliant Mechanisms with Hinge-Free Characteristic and Totally Decoupled Kinematics

Shouyu Cai ¹, Wenshang Zhou ¹, Hongtao Wei ^{1,*} and Mingfu Zhu ^{2,*}¹ School of Mechanics and Safety Engineering, Zhengzhou University, Zhengzhou 450001, China² School of Physics and Microelectronic, Zhengzhou University, Zhengzhou 450001, China

* Correspondence: htwei@zzu.edu.cn (H.W.); zhumingfu@zzu.edu.cn (M.Z.)

Abstract: A new multi-constraint optimization model with the weighted objective function is proposed to design the multi-input-multi-output (MIMO) compliant mechanisms. The main feature of this work is that both the two notable problems related to the de facto hinge and the movement coupling are tackled simultaneously in the topological synthesis of MIMO compliant mechanisms. To be specific, the first problem is the severe stress concentration in the flexible hinge areas, and it is solved by the introduction of input and output compliances into the objective function, which could facilitate the optimization to strike a good balance between structural flexibility and stiffness. The second problem is the high degree of control complexity caused by the coupled outputs and inputs, and it is addressed by achieving the complete decoupling with two groups of extra constraints that are used to suppress the input coupling and the output coupling, respectively. As the most common and effective topology optimization method, the Solid Isotropic Material with Penalization (SIMP)-based density method is adopted here to obtain the optimized configurations. After the analytical sensitivity deduction related to the weighted objective function and constraints, two typical numerical examples are presented to demonstrate the validity of the proposed topology optimization framework in designing the hinge-free and completely decoupled MIMO compliant mechanisms.

Keywords: topology optimization; compliant mechanism; de facto hinge; movement coupling; multiple inputs; multiple outputs



Citation: Cai, S.; Zhou, W.; Wei, H.; Zhu, M. Topology Optimization Design of Multi-Input-Multi-Output Compliant Mechanisms with Hinge-Free Characteristic and Totally Decoupled Kinematics. *Appl. Sci.* **2023**, *13*, 4627. <https://doi.org/10.3390/app13074627>

Academic Editors: Qi Xia, Hui Liu and Kai Long

Received: 4 February 2023

Revised: 3 April 2023

Accepted: 4 April 2023

Published: 6 April 2023



Copyright: © 2023 by the authors. Licensee MDPI, Basel, Switzerland. This article is an open access article distributed under the terms and conditions of the Creative Commons Attribution (CC BY) license (<https://creativecommons.org/licenses/by/4.0/>).

1. Introduction

Compliant mechanisms, unlike the conventional rigid-body mechanisms, gain their mobility from the deflection of flexible members rather than from movable joints, and therefore have many intrinsic advantages, such as no lubrication, low wear, light weight, ease in assembly and miniaturization [1–3]. Nowadays, compliant mechanisms outperform the rigid-body ones in various applications including micro/nano-electro-mechanical systems (MEMS/NEMS), high-precision instruments and biomedical electronic devices [4,5].

The advantages of compliant mechanisms have aroused considerable and increasing interest in synthesis methods of compliant mechanisms that can be classified into two main categories: kinematic-based approaches [6,7] and structural topology optimization approaches [8,9]. The design method adopted in this work belongs to the latter category, because the topology optimization technique, which could facilitate designers to break through traditional institutions and experience, has already proven to be a powerful tool to obtain competitive and innovative mechanical and architectural structures [10–12].

Topology optimization has undergone tremendous development since the homogenization method was proposed [13], and now it can be realized by many excellent methods, including density method [14–17], evolutionary method [18–23], level set method [24–29], bubble method [30,31], feature-driven method [32–34], moving morphable components

method [35–37] and several others [38–44]. It is worth noting that the Evolutionary Topology Optimization (ETO) approach [22] not only belongs to the evolutionary method, but also is an elemental volume fraction-based method proposed for the first time, which also includes the Smooth-Edged Material Distribution for Optimizing Topology (SEMDOT) algorithm [45]. Among the various topology optimization approaches, the density method with Solid Isotropic Material with Penalization (SIMP) interpolation scheme is the most widely used one, mainly because of its clear physical conception, simple formula, excellent numerical stability and convergence. In this paper, the SIMP approach is adopted to synthesize compliant mechanisms, and the corresponding compliant mechanism design problem is converted into the problem of seeking the optimal material distribution within a given design domain [2].

In the topology optimization design of compliant mechanisms, there are some challenging problems that prevent optimized results from being widely applied to the engineering practice, and the present work focuses on solving the two most common and important problems: de facto hinges and movement coupling.

The former problem is reflected in Figure 1; de facto hinges (i.e., flexure points [46]) make the resulting mechanism not actually compliant but function as the rigid-body one with revolute joints [47,48]. To be more specific, if the compliant mechanism is loaded, its major part will essentially undergo the rigid-body motion, and the mechanical deflection can only be realized by the bending deformations around its de facto hinges. Consequently, energy and force are mainly transmitted through the bending of flexible hinges, where the severe local stress concentration occurs unavoidably and may significantly shorten the mechanical life span [4–7,49–51].

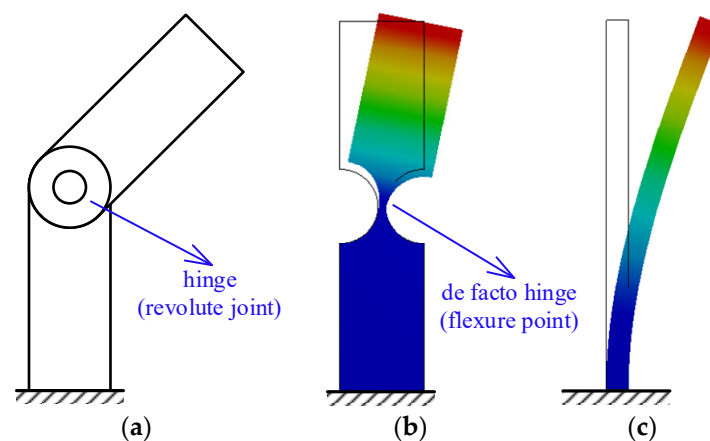


Figure 1. Drawings related to the de facto hinge phenomenon: (a) the revolute joint of two rigid bodies; (b) the flexure point of a structure; (c) the distributed compliant mechanism.

In order to eliminate de facto hinges and obtain the virtually distributed compliant mechanism [52,53], varieties of methods have been developed and some characteristic ones are described below. Luo et al. [54] address the de facto hinge problem by introducing a quadratic energy functional used in image analysis in the level set method; Pereira and Cardoso [55] study the joint use of local stress constraints and proper filter radius to design distributed compliant mechanisms; Dunning [56] removes de facto hinges by applying minimum length-scale constraints to both structure and void regions; Zhan and Luo [57] prevent the formation of flexible hinges by means of the robust topology optimization considering material uncertainties. In our work, a relatively popular method with the weighted objective function is adopted, in which the optimization objective includes geometric and mechanical advantages [46,47]. The geometric advantage usually represented by the desired output displacement or the mutual compliance is employed to quantify the mechanical performance and enhance the output motion. The mechanical

advantage that could be simply defined by the mean compliance is used to ensure adequate structural stiffness and hence has the effect of eliminating de facto hinges [58,59].

The latter problem is the coupling issue of outputs and inputs existing in the operational process of multi-input-multi-output (MIMO) compliant mechanisms [60–65]. The output coupling always results in complex kinematic models, and the input coupling would lead to undesired loads on actuators. Both of them could cause serious difficulty in motion control, so the decoupling property is a crucial factor needing to be considered in the process of designing precision MIMO compliant mechanisms. In the current study, we aim to develop fully decoupled mechanisms with both output and input decoupling properties. Generally, the output decoupling means one actuator produced only one axial output motion without affecting the motion of other axes [61], and the input decoupling emphasizes on the isolation of actuations [62]. In order to obtain the fully decoupled compliant mechanism, many effective kinematic-based approaches have already been proposed [63–65], but they often lead to complicated structures that are not convenient for control implementation and prototype fabrication. To solve this problem, Zhu et al. [60] adopted the topology optimization method to design the fully decoupled compliant mechanism, and relatively simple structures with de facto hinges were obtained.

The present study is conducted to design hinge-free and fully-decoupled MIMO compliant mechanisms, by addressing both the de facto hinge and the movement coupling problems at the same time. To achieve this end, a new multi-objective-multi-constraint optimization model is proposed. Specifically, the multi-objective function consists of desired output displacements as well as input and output compliances, and corresponding weighting factors are updated adaptively to make the optimization strike a good balance between structural flexibility and stiffness. The multi-constraint conditions could be classified into output decoupling and input decoupling constraints, which are employed to restrict the undesired displacements at output and input ports, respectively. In order to solve the above-described optimization model, analytical sensitivities related to multi-objective and constraint functions are deduced and the Method of Moving Asymptotes (MMA) [66] is used as the optimizer. It should be noted that the proposed method is quite convenient as it possesses a self-adaptive ability and does not need the setting of many empirical parameters, such as stiffness coefficients of connecting springs.

The remainder of the paper is organized as follows. MIMO compliant mechanism design problems regarding the de facto hinge and the movement coupling are introduced in Section 2, where the integrated mathematical model of concerned optimization problems is built. Based on this optimization model, Section 3 conducts the sensitivity analysis and provides the optimization implementation. In Section 4, numerical examples of a path-generating mechanism and an inverter are presented to demonstrate the validity of the proposed method. Finally, conclusions are addressed.

2. Problem Formulation

2.1. Topology Optimization Approach

The continuum structural topology optimization can be seen as finding the optimal material distribution within a given design domain. As the most widely used topology optimization approach, the density method regards elements for analysis as basic design units, with which the design domain is discretized. The existence of material in the e th element is measured by its density x_e ranging from 0 to 1, and $x_e = 1$ or 0 means that the e th element is the solid or void one. In order to suppress the occurrence of elements with intermediate densities (i.e., $0 < x_e < 1$) in the final design, the following modified SIMP interpolation scheme is adopted:

$$E_e = E(x_e) = E_{\min} + x_e^p(E_0 - E_{\min}), \quad x_e \in [0, 1] \quad (1)$$

where E_e denotes Young's modulus of the e th element material, E_0 and E_{\min} denote Young's moduli of solid and void materials, respectively, and E_{\min} takes a minimal positive number

to avoid singularity of the stiffness matrix; p is a penalization factor introduced to ensure black-and-white solutions and it is typically set to 3.

According to the SIMP based density method, the global stiffness matrix K is calculated by

$$K = \sum_{e=1}^N E_e k \tag{2}$$

where k is the element stiffness matrix for an element with unit Young’s modulus, and N is the total number of elements used to discretize the design domain.

2.2. Objective Function with the Effect of Eliminating De Facto Hinges

Figure 2 shows the design domain D and boundary conditions of a typical MIMO compliant mechanism, in which each input load is responsible for actuating a specific output displacement, i.e., the desired output displacement u_{O_i} at the i th output port O_i should be generated by applying an input force F_{I_i} at the corresponding input port I_i ($i = 1, 2, \dots, n$).

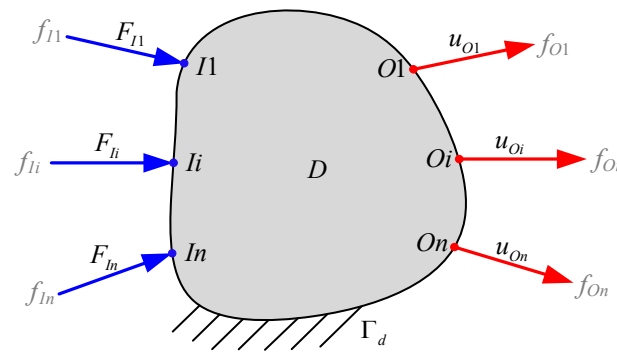


Figure 2. Design domain and boundary conditions of a MIMO compliant mechanism.

In this work, the output displacement u_{O_i} produced by F_{I_i} is calculated by using the concept of the mutual mean compliance as follows:

$$u_{O_i} = V_{O_i}^T K U_{I_i} \tag{3}$$

where U_{I_i} is the displacement vector associated with the input force F_{I_i} , and V_{O_i} is the displacement vector due to a virtual unit load f_{O_i} that is applied at the output point O_i and has the same direction with u_{O_i} (see Figure 2).

The core design objective of compliant mechanisms is to maximize the desired output displacements, and it could be formulated as: Minimize $-u_{O_i}$ ($i = 1, 2, \dots, n$). This multi-objective formulation could be transformed into the following single-objective one via the weighted sum method:

$$\text{Minimize : } J = -\sum_{i=1}^n \omega_i u_{O_i} \tag{4}$$

in which ω_i is the weighting factor of u_{O_i} and is updated with iterations using

$$\omega_i^{iter} = \begin{cases} 1 & i = 1 \text{ or } iter = 1 \\ \left| \frac{u_{O_i}^{iter-1}}{u_{O_i}^{iter-1}} \right| & i \geq 1 \text{ and } iter \geq 2 \end{cases} \tag{5}$$

where superscripts $iter$ and $iter - 1$ denote $iter$ th and $(iter - 1)$ th iteration, respectively. It should be noted that de facto hinges are very likely to appear in design results if the objective function only involves output displacements, as shown in Equation (4).

In order to eliminate de facto hinges naturally, the present optimization work is dedicated to striking a good balance between structural flexibility and stiffness. The stiffness

of compliant mechanisms could be measured by the input compliance C_{Ii} and the output compliance C_{Oi} defined as

$$C_{Ii} = \mathbf{V}_{Ii}^T \mathbf{K} \mathbf{V}_{Ii} \tag{6}$$

$$C_{Oi} = \mathbf{V}_{Oi}^T \mathbf{K} \mathbf{V}_{Oi} \tag{7}$$

where \mathbf{V}_{Ii} is the displacement vector due to a virtual unit load f_{Ii} with the same input point and direction as F_{Ii} . The smaller the compliance is, the larger the mechanism stiffness is.

After the introduction of input and output compliances (C_{Ii} and C_{Oi}) computed by Equations (6) and (7) into the objective function (4), the new formulation based on the weighted sums of the flexibility and stiffness is developed as

$$\text{Minimize : } J = -\sum_{i=1}^n \omega_i u_{Oi} + \sum_{i=1}^n w_{Ii} C_{Ii} + \sum_{i=1}^n w_{Oi} C_{Oi} \tag{8}$$

in which w_{Ii} and w_{Oi} are the weighting factors of C_{Ii} and C_{Oi} , respectively. Similar to the factor ω_i , both the w_{Ii} and w_{Oi} change with iterations adaptively as follows:

$$w_{Ii}^{iter} = \begin{cases} 1 & i = 1, iter = 1 \\ \left| \frac{u_{O1}^{iter-1}}{C_{Ii}^{iter-1}} \right| & i \geq 2, iter \geq 2 \end{cases} \tag{9}$$

$$w_{Oi}^{iter} = \begin{cases} 1 & i = 1, iter = 1 \\ \left| \frac{u_{O1}^{iter-1}}{C_{Oi}^{iter-1}} \right| & i \geq 2, iter \geq 2 \end{cases} \tag{10}$$

The reason for adopting these weighting factors ω_i , w_{Ii} and w_{Oi} is that values of weighted quantities u_{Oi} , C_{Ii} and C_{Oi} vary widely and always differ by orders of magnitude. The reason for adaptively adjusting them using Equations (5), (9) and (10) is that it can prevent some of these quantities from becoming insanely large. In other words, the adaptive update scheme helps to balance the flexibility and stiffness of compliant mechanisms, and distributed ones with no de facto hinges can therefore be obtained.

2.3. Constraint Functions Set for Achieving Complete Decoupling

A completely decoupled MIMO compliant mechanism implies that each input load produces only one directional output motion without affecting the motions at other ports. However, one input load usually leads to undesired output displacement at non-corresponding ports, which is known as coupling. If the motion appears at the non-corresponding output port, we will call it output coupling, as depicted in Figure 3a. If the motion exists in any other input port, we will call it input coupling, as depicted in Figure 3b. Coupling goes against the precision operation of mechanisms and must be prevented.

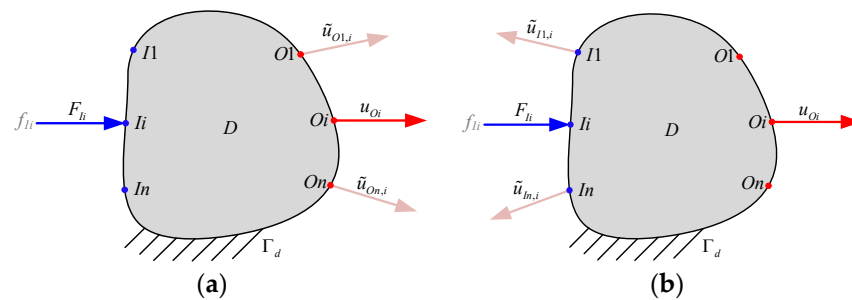


Figure 3. Schematic of the Output coupling (a) and the input coupling (b) produced by F_{Ii} .

In Figure 3, a load F_{Ii} is applied at the i th input port Ii and produces a desired displacement u_{Oi} at the output port Oi , whereas in the meantime, the coupled displacements at other ports are unavoidably generated, which are denoted by $\tilde{u}_{Oj,i}$ and $\tilde{u}_{Ij,i}$. The former means

the displacement at the output point O_j ($j \neq i$) produced by F_{li} , and the latter represents the displacement at the input point I_j ($j \neq i$) produced by F_{li} . To overcome the coupling issue, the following extra constraints are introduced into the optimization formulation:

$$\delta_{j,i} = \left(\frac{\tilde{u}_{Oj,i}}{u_{O_i}} \right)^2 \leq [\delta] \tag{11}$$

$$\gamma_{j,i} = \left(\frac{\tilde{u}_{Ij,i}}{u_{O_i}} \right)^2 \leq [\gamma] \tag{12}$$

where $\delta_{j,i}$ and $\gamma_{j,i}$ denote the output coupling index at O_j ($j \neq i$) and the input coupling index at I_j ($j \neq i$) due to F_{li} at I_i , respectively; both $[\delta]$ and $[\gamma]$ take very small positive numbers in order to suppress the movement coupling.

2.4. Optimization Model

By combining Equations (8), (11) and (12), one can obtain the mathematical model related to the topology optimization design of hinge-free and fully decoupled MIMO compliant mechanisms as follows:

$$\begin{aligned} \text{Minimize : } J &= - \sum_{i=1}^n \omega_i u_{O_i} + \sum_{i=1}^n w_{I_i} C_{I_i} + \sum_{i=1}^n w_{O_i} C_{O_i} \\ \text{Subject to : } \delta_{j,i} &= \left(\frac{\tilde{u}_{Oj,i}}{u_{O_i}} \right)^2 \leq [\delta] \\ \gamma_{j,i} &= \left(\frac{\tilde{u}_{Ij,i}}{u_{O_i}} \right)^2 \leq [\gamma] \\ \frac{V}{V_0} &= \sum_{e=1}^N v_e x_e / V_0 \leq f \\ \mathbf{KU}_I &= \mathbf{F}_I, \mathbf{KV}_I = \mathbf{f}_I, \mathbf{KV}_O = \mathbf{f}_O \\ 0 < x_{\min} &\leq x_e \leq 1; e = 1, 2, \dots, N \\ i &= 1, 2, \dots, n; j = 1, 2, \dots, i - 1, i + 1, \dots, n \end{aligned} \tag{13}$$

In which V and V_0 are, respectively, the volumes of the optimized structure and the design domain; v_e is the e th element volume; f is the prescribed volume fraction; $\mathbf{F}_I, \mathbf{f}_I$ and \mathbf{f}_O are the global load matrices of which the i th columns are formed by the external load F_{li} , virtual unit loads f_{li} and f_{oi} ($i = 1, 2, \dots, n$), respectively; $\mathbf{U}_I, \mathbf{V}_I$ and \mathbf{V}_O are the corresponding global displacement matrices, whose i th columns are respectively $\mathbf{U}_{li}, \mathbf{V}_{li}$ and \mathbf{V}_{oi} defined as before.

3. Sensitivity Analysis and Optimization Implementation

3.1. Sensitivity Analysis

Sensitivity analysis is usually implemented as an essential step in structural optimization for the following reasons: to provide the information about how sensitive the objective function is with respect to design variables; to solve optimization problems via efficient gradient-based topology algorithms; to carry out the sensitivity filtering scheme, and so on.

The sensitivity of the objective function J defined in Equation (13) can be computed by solving its partial differentiation to the design variable x_e as

$$\begin{aligned} \frac{\partial J}{\partial x_e} &= - \sum_{i=1}^n \omega_i \frac{\partial u_{O_i}}{\partial x_e} + \sum_{i=1}^n w_{I_i} \frac{\partial C_{I_i}}{\partial x_e} + \sum_{i=1}^n w_{O_i} \frac{\partial C_{O_i}}{\partial x_e} \\ &= \sum_{i=1}^n \omega_i \mathbf{V}_{O_i}^T \frac{\partial \mathbf{K}}{\partial x_e} \mathbf{U}_{I_i} - \sum_{i=1}^n w_{I_i} \mathbf{V}_{I_i}^T \frac{\partial \mathbf{K}}{\partial x_e} \mathbf{V}_{I_i} - \sum_{i=1}^n w_{O_i} \mathbf{V}_{O_i}^T \frac{\partial \mathbf{K}}{\partial x_e} \mathbf{V}_{O_i} \\ &= p x_e^{p-1} (E_0 - E_{\min}) \left[\sum_{i=1}^n \omega_i \mathbf{V}_{O_i}^T \mathbf{kU}_{I_i} - \sum_{i=1}^n w_{I_i} \mathbf{V}_{I_i}^T \mathbf{kV}_{I_i} - \sum_{i=1}^n w_{O_i} \mathbf{V}_{O_i}^T \mathbf{kV}_{O_i} \right] \end{aligned} \tag{14}$$

It is worth mentioning that weighting factors ω_i, w_{I_i} and w_{O_i} remain constant in the current optimization iteration, so their sensitivities are not involved in the above equation.

The sensitivity of the output coupling constraint function $\delta_{j,i}$ with respect to x_e could be calculated as

$$\begin{aligned} \frac{\partial \delta_{j,i}}{\partial x_e} &= \partial \left(\frac{\tilde{u}_{Oj,i}}{u_{Oi}} \right)^2 / \partial x_e \\ &= 2 \frac{\tilde{u}_{Oj,i}}{u_{Oi}} \left(\frac{\partial \tilde{u}_{Oj,i}}{\partial x_e} u_{Oi} - \tilde{u}_{Oj,i} \frac{\partial u_{Oi}}{\partial x_e} \right) \\ &= 2 \frac{\mathbf{v}_{Oj,i}^T \mathbf{K} \mathbf{u}_{li}}{\mathbf{v}_{Oj,i}^T \mathbf{K} \mathbf{u}_{li}} \left(\frac{-V_{Oj,i} \frac{\partial \mathbf{K}}{\partial x_e} \mathbf{u}_{li} \cdot \mathbf{v}_{Oj,i}^T \mathbf{K} \mathbf{u}_{li} - \mathbf{v}_{Oj,i}^T \mathbf{K} \mathbf{u}_{li} \cdot (-\mathbf{v}_{Oj,i}^T \frac{\partial \mathbf{K}}{\partial x_e} \mathbf{u}_{li})}{(\mathbf{v}_{Oj,i}^T \mathbf{K} \mathbf{u}_{li})^2} \right) \\ &= 2 p x_e^{p-1} (E_0 - E_{\min}) \frac{\mathbf{v}_{Oj,i}^T \mathbf{K} \mathbf{u}_{li} (\mathbf{v}_{Oj,i}^T \mathbf{K} \mathbf{u}_{li} \cdot \mathbf{v}_{Oj,i}^T \mathbf{K} \mathbf{u}_{li} - V_{Oj,i} \mathbf{K} \mathbf{u}_{li} \cdot \mathbf{v}_{Oj,i}^T \mathbf{K} \mathbf{u}_{li})}{(\mathbf{v}_{Oj,i}^T \mathbf{K} \mathbf{u}_{li})^3} \end{aligned} \tag{15}$$

Similarly, the sensitivity of the input coupling constraint function $\gamma_{j,i}$ can be derived as

$$\begin{aligned} \frac{\partial \gamma_{j,i}}{\partial x_e} &= \partial \left(\frac{\tilde{u}_{Ij,i}}{u_{Oi}} \right)^2 / \partial x_e \\ &= 2 \frac{\tilde{u}_{Ij,i}}{u_{Oi}} \left(\frac{\partial \tilde{u}_{Ij,i}}{\partial x_e} u_{Oi} - \tilde{u}_{Ij,i} \frac{\partial u_{Oi}}{\partial x_e} \right) \\ &= 2 p x_e^{p-1} (E_0 - E_{\min}) \frac{\mathbf{v}_{Ij,i}^T \mathbf{K} \mathbf{u}_{li} (\mathbf{v}_{Ij,i}^T \mathbf{K} \mathbf{u}_{li} \cdot \mathbf{v}_{Oj,i}^T \mathbf{K} \mathbf{u}_{li} - V_{Ij,i} \mathbf{K} \mathbf{u}_{li} \cdot \mathbf{v}_{Oj,i}^T \mathbf{K} \mathbf{u}_{li})}{(\mathbf{v}_{Oj,i}^T \mathbf{K} \mathbf{u}_{li})^3} \end{aligned} \tag{16}$$

3.2. Optimization Implementation

The design domain is discretized by four-node bilinear elements. Numerical instabilities involved in the optimization process, such as the checkerboard pattern and the mesh dependence, are addressed by the sensitivity-based filter method [15]. The sensitivity filter radius is set to 1.5 times the element size. The present multi-constraint optimization problem is solved by using the well-known method of moving asymptotes (MMA) [66]. The convergence criterion is that the maximum iteration number attains 2000 or the maximum variation of design variables is less than 0.01.

Here, we summarize the optimization procedure for the topology optimization of MIMO compliant mechanisms in this paper as follows:

- Step 1. Make an initialization by setting initial values for parameters.
- Step 2. Carry out the finite element analysis (FEA) to obtain u_{Oi} , $\tilde{u}_{Oj,i}$, $\tilde{u}_{Ij,i}$, C_{li} and $C_{Oj,i}$.
- Step 3. Calculate ω_i , w_{li} and $w_{Oj,i}$ by Equations (5), (9) and (10), respectively.
- Step 4. Compute and then filter the sensitivities related to the design problem (13).
- Step 5. Update design variables by the method of moving asymptotes (MMA).
- Step 6. Check for convergence. If not converge, go to Step 2.

4. Experimental Validations

Two design examples of MIMO compliant mechanisms are tested to verify the validity of the proposed method. The same prescribed volume fraction with $f = 0.3$, the same density for void element $x_{\min} = 10^{-4}$ as well as the same material properties with Poisson's ratio $\nu = 0.3$, Young's moduli for solid material $E_0 = 1$ and for void material $E_{\min} = 10^{-9}$ are adopted in both cases.

4.1. Compliant Path Generator

The design domain and boundary conditions of the compliant path generator are plotted in Figure 4. Two input forces F_{I1} and F_{I2} that are applied at input points $I1$ and $I2$ lead to output displacements u_{O1} and u_{O2} at the same output point $O1(O2)$, respectively. The void areas at the right top and the right bottom corners have the same size of 40×40 .

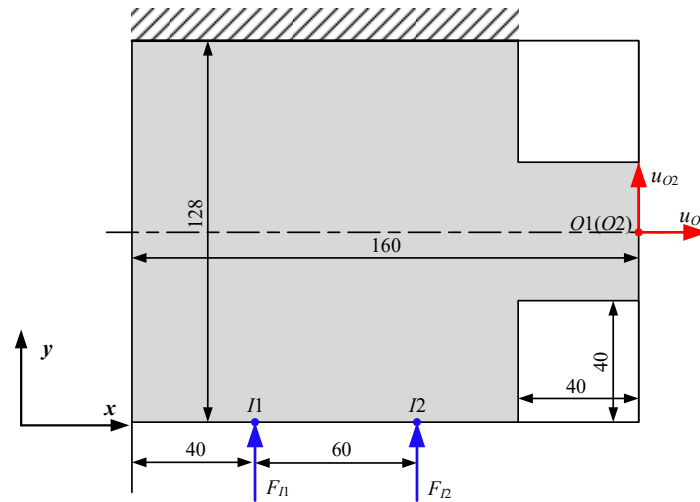


Figure 4. Design domain and boundary conditions of the compliant path generator.

4.1.1. Validity of the Hinge-Free Design Scheme

For comparison purposes, the traditional optimization design model of compliant mechanisms is first provided as follows:

$$\begin{aligned}
 \text{Minimize : } & J = - \sum_{i=1}^n \omega_i u_{O_i} \\
 \text{Subject to : } & V/V_0 \leq f \\
 & \mathbf{KU} = \mathbf{F} \\
 & 0 < x_{\min} \leq x_e \leq 1 \\
 & e = 1, 2, \dots, N \\
 & i = 1, 2, \dots, n
 \end{aligned} \tag{17}$$

where \mathbf{K} differs from that in Equation (13) due to the adoption of the spring model and is expressed as

$$\mathbf{K} = \sum_{e=1}^N E_e \mathbf{k} + \sum_{i=1}^n (\mathbf{K}_{I_i} + \mathbf{K}_{O_i}) \tag{18}$$

in which \mathbf{K}_{I_i} and \mathbf{K}_{O_i} denote the global stiffness matrices related to the input spring at input point I_i and output spring at output point O_i , respectively. In this test, the stiffness coefficients of input and output springs are all set to 0.1.

To verify the effectiveness of the objective function defined by Equation (8) in eliminating de facto hinges, the proposed optimization model (13) without considering coupling constraints is adopted here as

$$\begin{aligned}
 \text{Minimize : } & J = - \sum_{i=1}^n \omega_i u_{O_i} + \sum_{i=1}^n w_{I_i} C_{I_i} + \sum_{i=1}^n w_{O_i} C_{O_i} \\
 \text{Subject to : } & \frac{V}{V_0} = \sum_{e=1}^N v_e x_e / V_0 \leq f \\
 & \mathbf{KU}_I = \mathbf{F}_I, \mathbf{KV}_I = \mathbf{f}_I, \mathbf{KV}_O = \mathbf{f}_O \\
 & 0 < x_{\min} \leq x_e \leq 1; e = 1, 2, \dots, N \\
 & i = 1, 2, \dots, n \\
 & j = 1, 2, \dots, i - 1, i + 1, \dots, n
 \end{aligned} \tag{19}$$

The design results of the path generator related to optimization models (17) and (19) are shown in Figure 5a,b, respectively. Both results have reasonable load paths for this compliant mechanism with two inputs and two outputs, even if their topologies are significantly different. Figure 6 plots the corresponding strain energy density distributions.

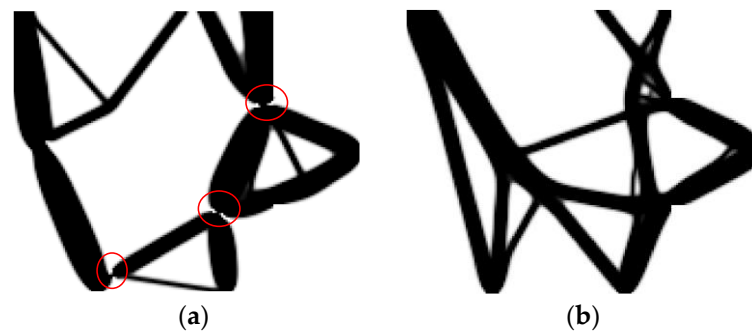


Figure 5. Design results obtained by using optimization models (a) Equation (17) and (b) Equation (19).

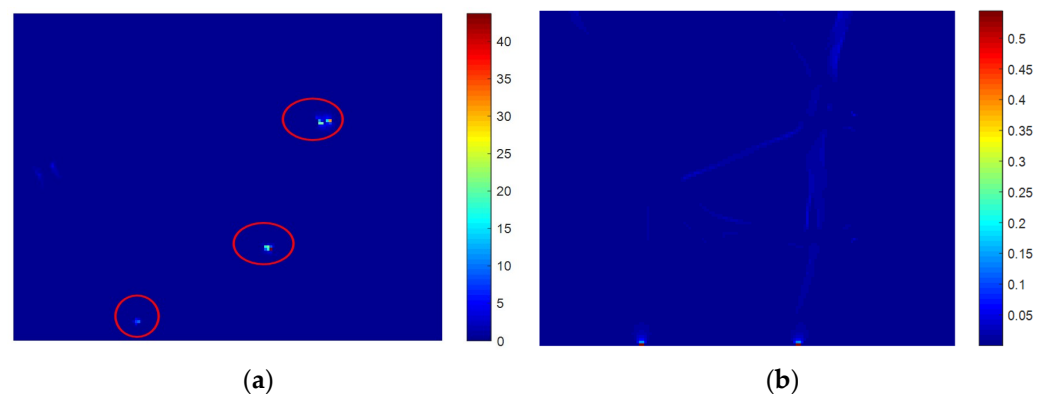


Figure 6. Plots of the resulting strain energy densities related to optimization modes (a) Equation (17) and (b) Equation (19).

The optimized path generator in Figure 5a is the lumped compliant mechanism as it contains several de facto hinges, around which the values of strain energy density are pretty large, as shown in Figure 6a. It can be seen from Figures 5b and 6b that there are no slender hinges with high strain energy density in the design result, which means that the path generator optimized by using the objective function (8) is the hinge-free compliant mechanism (i.e., the distributed compliant mechanism).

4.1.2. Validity of Decoupling Constraint Functions

In this section, we further investigate the effect of coupling constraints on achieving full decoupling. Figure 7 plots the horizontal and vertical displacement distributions of the design result shown in Figure 5b under different load cases F_{I1} and F_{I2} . Figure 8 draws the same type of displacement distributions related to the design result optimized using the optimization mode (13) with coupling constraints. Note that the two permissible coupling indices $[\delta]$ and $[\gamma]$ involved in Equation (13) are both set to 0.01 here. Figure 9 shows the evolution of the structural configuration optimized using Equation (13), and Figure 10 plots the convergence histories.

From Figures 7 and 8, one could visually determine whether the coupling of inputs or outputs exists or not. As depicted in Figure 7b, the undesired vertical displacement at the output point is produced by the load $F_{I1} = 1$, and this output coupling issue is successfully solved in Figure 8b. In addition, Figure 7c shows unexpected horizontal displacements at the output point and the input point $I1$, and the latter is exceptionally large, both of which are well suppressed in Figure 8c. Desired horizontal and vertical displacements at the output point $O1(O2)$ are exhibited in Figures 7a,b and 8a,b, from which we could see that the design result with totally decoupled kinematics has almost the same expected output displacements as the one with the movement coupling issue.

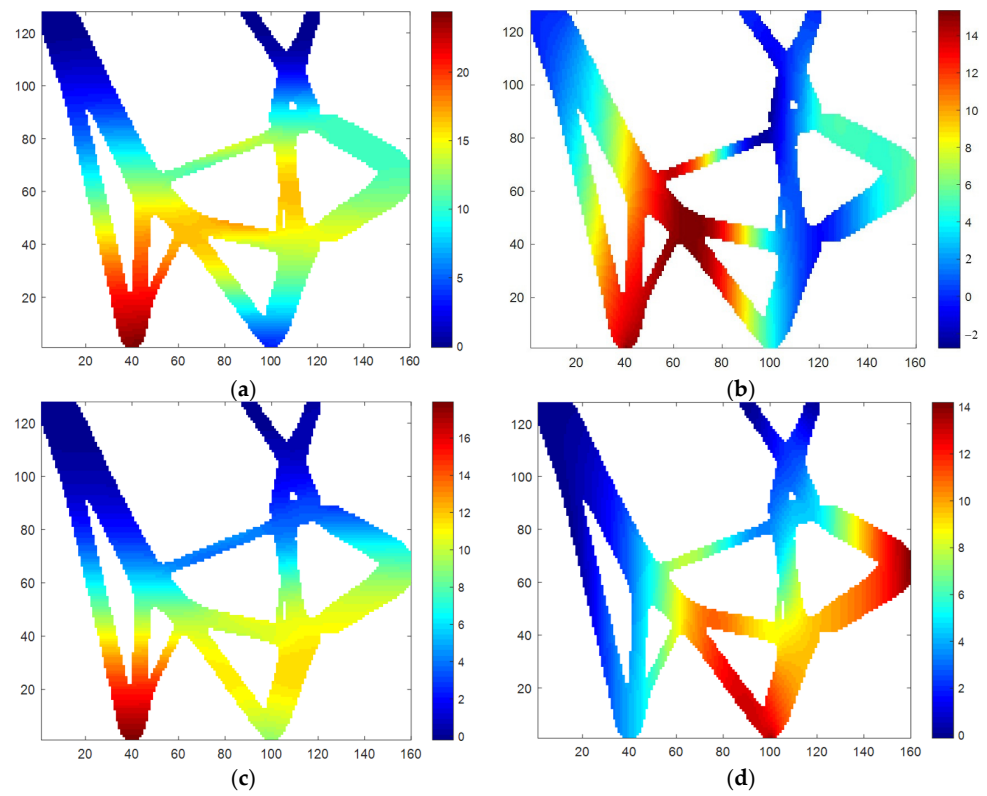


Figure 7. Obtained displacement distributions using Equation (19): (a) horizontal and (b) vertical displacement results generated by F_{11} , (c) horizontal and (b) vertical displacement results generated by F_{12} .

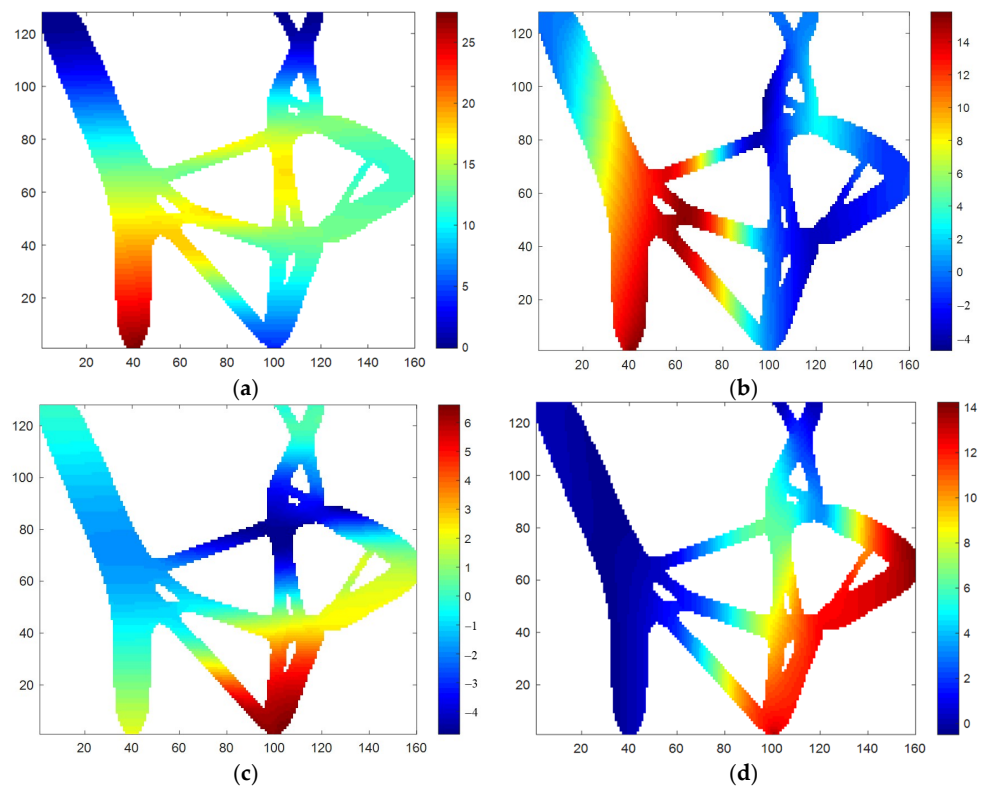


Figure 8. Obtained displacement distributions using Equation (13): (a) horizontal and (b) vertical displacement results generated by F_{11} , (c) horizontal and (d) vertical displacement results generated by F_{12} .

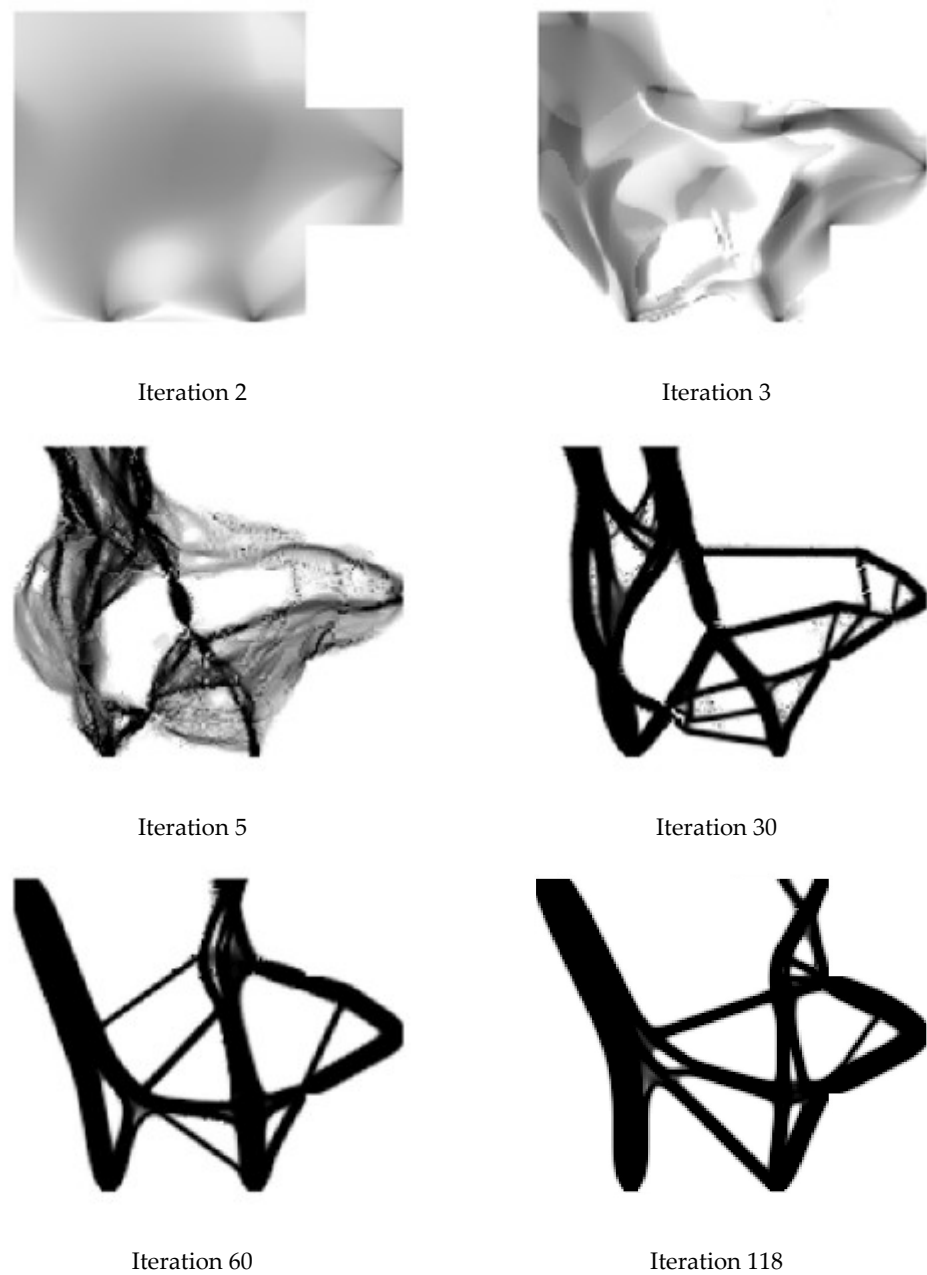


Figure 9. Evolution of the structural configuration optimized using Equation (13).

Tables 1 and 2 provide the exact values of desired and undesired displacements as well as output and input coupling indices, and we can evaluate the output performances of the two design results shown in Figures 7 and 8 quantitatively. The absolute values of all the undesired displacements $\tilde{u}_{O2,1}$, $\tilde{u}_{I2,1}$, $\tilde{u}_{O1,2}$ and $\tilde{u}_{I1,2}$ related to the path generator drawn in Figure 8 decrease significantly, and accordingly the values of the coupling indices $\delta_{2,1}$, $\delta_{1,2}$, $\gamma_{2,1}$ and $\gamma_{1,2}$ are all quite small and not bigger than $[\delta] = [\gamma] = 0.01$. Such results manifest that both input and output couplings are under control.

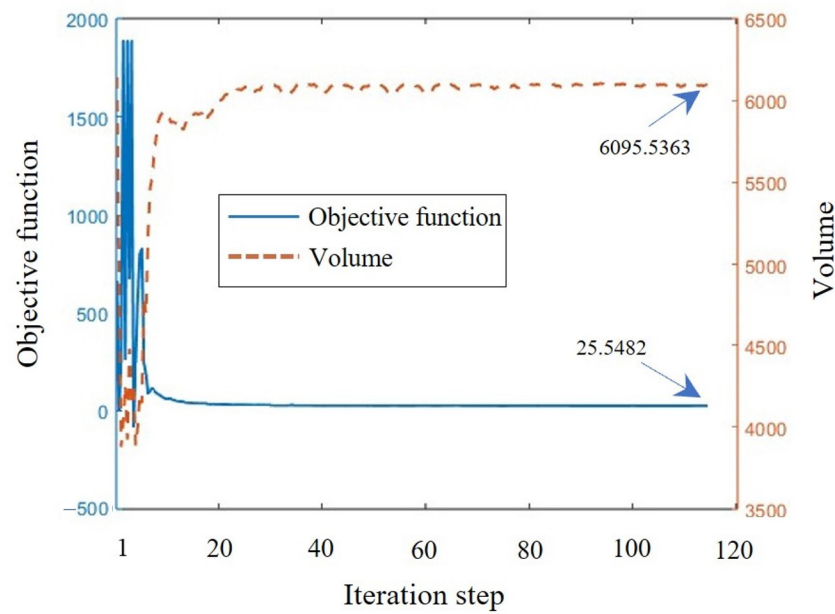


Figure 10. Convergence histories of the optimization using Equation (13).

Table 1. Desired and undesired displacements of design results shown in Figures 7 and 8.

	u_{O1}	$\tilde{u}_{O2,1}$	$\tilde{u}_{I2,1}$	u_{O2}	$\tilde{u}_{O1,2}$	$\tilde{u}_{I1,2}$
Figure 7	11.1167	6.0066	4.1642	14.3340	8.4481	4.1642
Figure 8	11.7840	-1.1522	0.0633	14.2408	1.4234	1.4234

Table 2. Output and input coupling indices of design results shown in Figures 7 and 8.

	$\delta_{2,1}$	$\delta_{1,2}$	$\gamma_{2,1}$	$\gamma_{1,2}$
Figure 7	0.29195	0.34736	0.14032	0.08440
Figure 8	0.00956	0.00999	0.00003	0.00002

4.1.3. The Effect of Permissible Coupling Indices $[\delta]$ and $[\gamma]$

In this work, there are only two parameters $[\delta]$ and $[\gamma]$ that need to be set manually. Their influences on the design results are investigated here. Figure 11 plots four optimized designs obtained using the optimization model (13) with different values of $[\delta]$ and $[\gamma]$, and the design result shown in Figure 11b is just the one drawn in Figure 8. It can be seen that all of the optimized results have reasonable and similar topologies even if $[\delta]$ and $[\gamma]$ vary greatly.

The performance data of the resulting mechanisms is given in Tables 3 and 4. For different decoupling levels (i.e., different values of $[\delta]$ and $[\gamma]$), the desired displacements u_{O1} and u_{O2} have little difference, whereas the undesired displacements change significantly, so that the values of all the coupling indices could be strictly limited to $[\delta]$ and $[\gamma]$. These results indicate that the values of $[\delta]$ and $[\gamma]$ have an evident impact on the decoupling degree of resulting mechanisms. Both the input and output couplings of optimized mechanisms can be controlled very well and the completely decoupled mechanisms could be obtained by using the optimization model (13) with very small $[\delta]$ and $[\gamma]$.

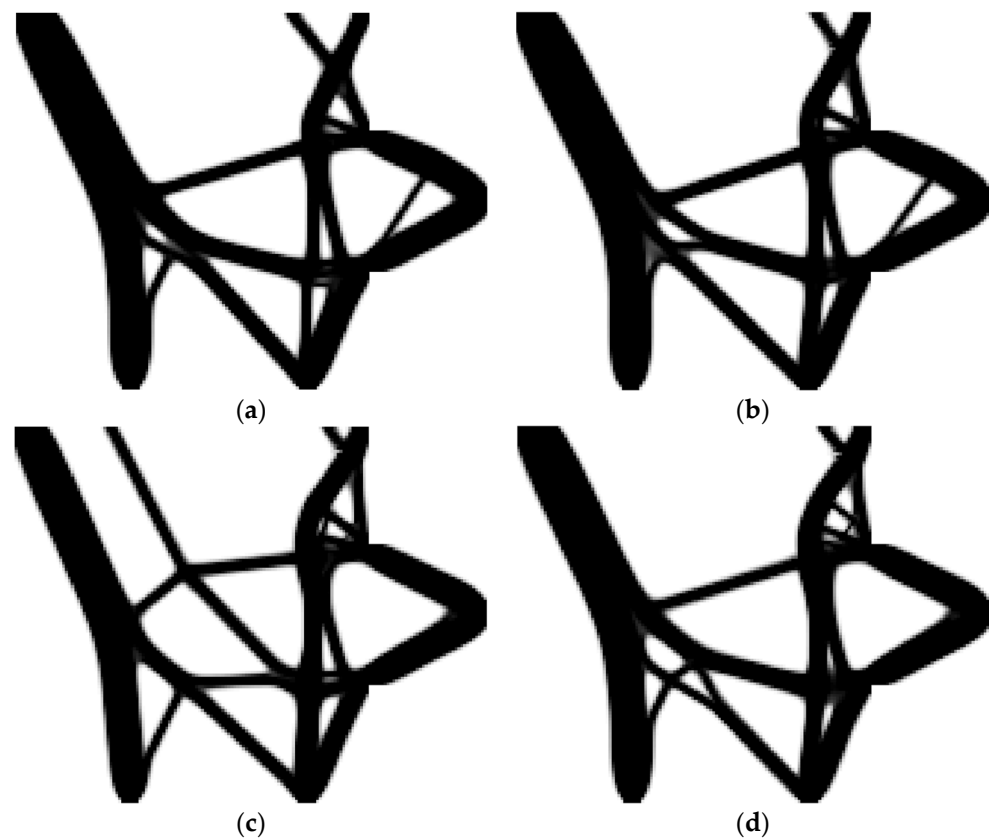


Figure 11. Path generators obtained with different $[\delta]$ and $[\gamma]$: (a) 0.1, (b) 0.01, (c) 0.001, (d) 0.0001.

Table 3. Desired and undesired displacements of the four design results shown in Figure 11.

	$[\delta] = [\gamma]$	u_{O1}	$\tilde{u}_{O2,1}$	$\tilde{u}_{I2,1}$	u_{O2}	$\tilde{u}_{O1,2}$	$\tilde{u}_{I1,2}$
Figure 11a	0.1	11.3304	2.1013	1.8679	14.2730	4.5116	1.8679
Figure 11b	0.01	11.7840	-1.1522	0.0633	14.2408	1.4234	1.4234
Figure 11c	0.001	12.6865	-0.4010	0.1077	14.2561	0.4506	0.1077
Figure 11d	0.0001	12.6229	-0.1262	-0.0631	14.2124	0.1421	-0.0631

Table 4. Output and input coupling indices of the four design results shown in Figure 11.

	$[\delta] = [\gamma]$	$\delta_{2,1}$	$\delta_{1,2}$	$\gamma_{2,1}$	$\gamma_{1,2}$
Figure 11a	0.1	0.03439	0.09991	0.02718	0.01713
Figure 11b	0.01	0.00956	0.00999	0.00003	0.00002
Figure 11c	0.001	0.00100	0.00100	0.00007	0.00006
Figure 11d	0.0001	0.00010	0.00010	0.00003	0.00002

4.2. Inverter

The design domain and boundary conditions are illustrated in Figure 12. The void areas at the right top and the right bottom corners have the same dimensions of 20×9 . Both the input point $I1$ and the output point $O1(O2)$ lie on the horizontal symmetry axis of the design domain. Input forces $F_{I1} = 1$ and $F_{I2} = 1$ are applied at input points $I1$ and $I2$, respectively. In addition, two output displacements u_{O1} and u_{O2} with the directions opposite to that of input forces are generated at the output point $O1(O2)$ correspondingly.

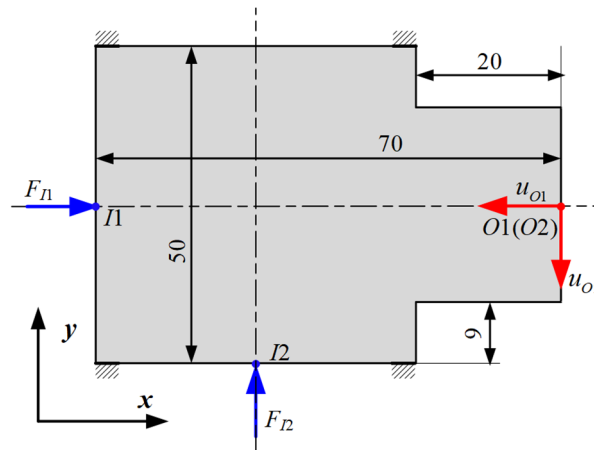


Figure 12. Design domain and boundary conditions of the inverter.

4.2.1. Eliminate De Facto Hinges

By adopting the traditional optimization model (17), the inverter with several de facto hinges shown in Figure 13a is obtained, and the local strain energy density with very large values occurred around these de facto hinges, as shown in Figure 13b. The strain energy distribution confirms that the flexibility of the obtained inverter is mainly provided by de facto hinges, which makes this inverter unavoidably suffer from the stress concentration problem.

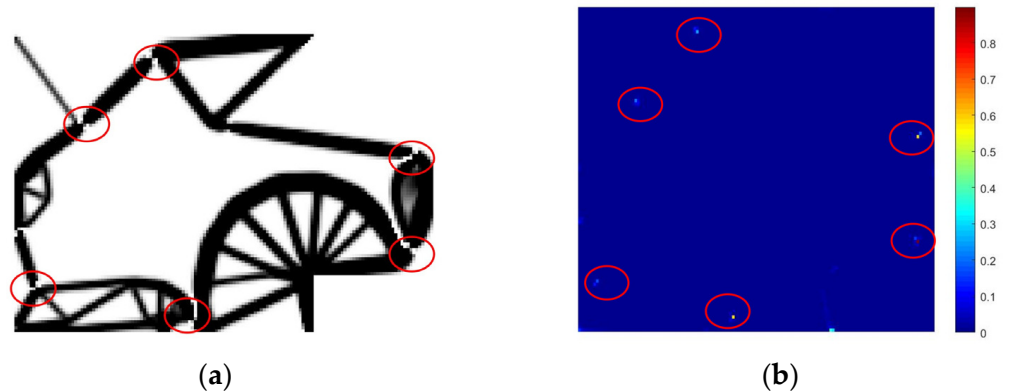


Figure 13. Design result of the inverter (a) using Equation (17) and the distribution of the local strain energy density (b).

The optimization mode (19) is employed here to eliminate de facto hinges, and the resulting inverter shown in Figure 14a almost has no hinges. The maximum value of the local strain energy density in the design domain except the fixed and input points is significantly reduced, as drawn in Figure 14b, so that the stress concentration decreases largely and the possible fatigue breakage is avoided to a great extent.

4.2.2. Achieve Complete Decoupling

This example adopts the optimization model (13) with the same four groups of values related to $[\delta]$ and $[\gamma]$ as in the previous example, i.e., $[\delta] = [\gamma] = 0.1$, $[\delta] = [\gamma] = 0.01$, $[\delta] = [\gamma] = 0.001$ and $[\delta] = [\gamma] = 0.0001$. The four different design results are plotted in Figure 15, and we can see that the four optimized topologies are obviously different.

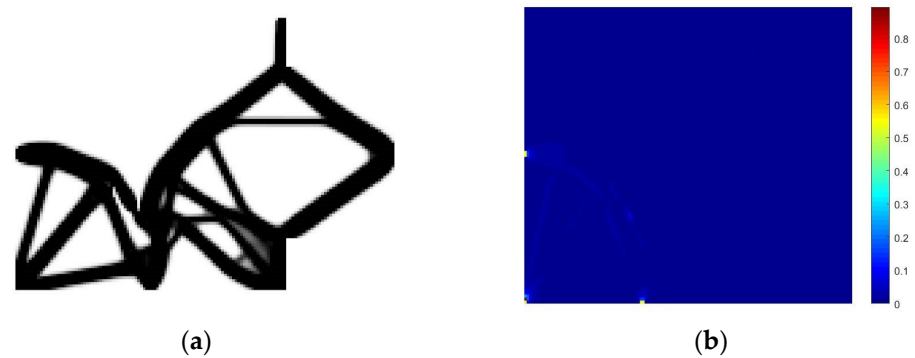


Figure 14. Design result of the inverter (a) using Equation (19) and the distribution of the local strain energy density (b).

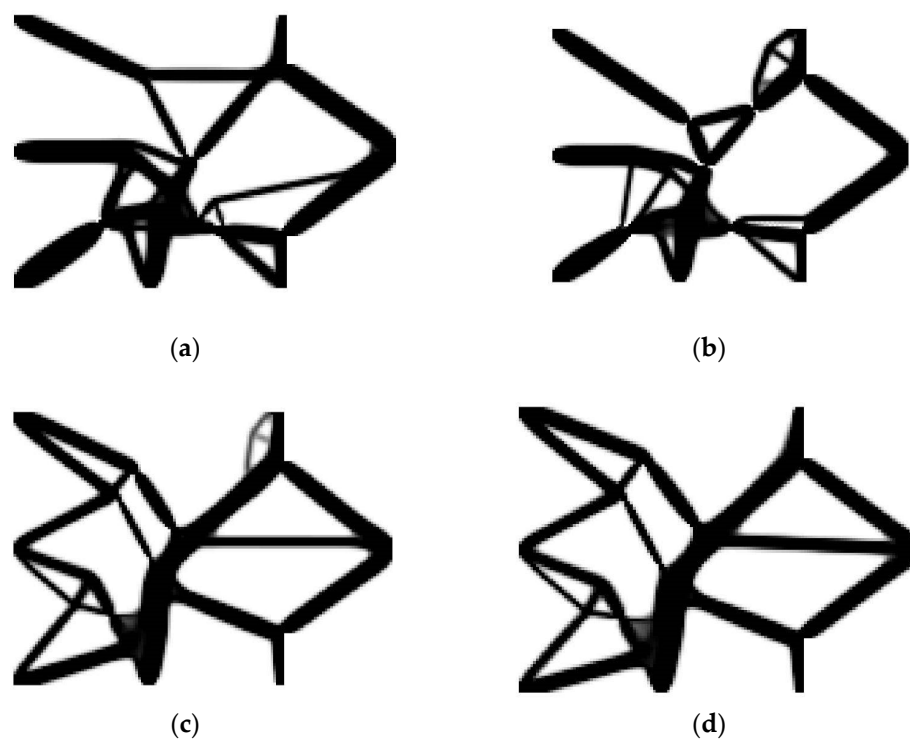


Figure 15. Inverters obtained with different $[\delta]$ and $[\gamma]$: (a) 0.1, (b) 0.01, (c) 0.001, (d) 0.0001.

Tables 5 and 6 list the values of concerned displacements and coupling indices of the design results shown in Figure 15. The desired displacements u_{O1} and u_{O2} are all negative, and it means the displacement inverter is successfully designed by using the proposed method. The smaller the values of $[\delta]$ and $[\gamma]$ are, the smaller the values of undesired displacements are. From the data in Table 6, one can learn that both the output and input coupling indices decrease greatly when $[\delta]$ and $[\gamma]$ become small, which are all strictly restricted within the permissible coupling indices $[\delta]$ and $[\gamma]$.

Table 5. Desired and undesired displacements of the four design results shown in Figure 15.

	$[\delta] = [\gamma]$	u_{O1}	$\tilde{u}_{O2,1}$	$\tilde{u}_{I2,1}$	u_{O2}	$\tilde{u}_{O1,2}$	$\tilde{u}_{I1,2}$
Figure 15a	0.1	−15.7907	−4.1756	4.9923	−24.1248	4.5064	4.9923
Figure 15b	0.01	−14.3172	−0.4670	−0.4670	−13.5221	1.0904	−0.4670
Figure 15c	0.001	−12.9474	−0.4063	−0.4063	−12.8545	0.4063	−0.4063
Figure 15d	0.0001	−17.5345	0.1752	0.1752	−17.8203	0.1781	0.1752

Table 6. Output and input coupling indices of the four design results shown in Figure 15.

	$[\delta] = [\gamma]$	$\delta_{2,1}$	$\delta_{1,2}$	$\gamma_{2,1}$	$\gamma_{1,2}$
Figure 15a	0.1	0.06992	0.03489	0.09995	0.04282
Figure 15b	0.01	0.01000	0.00650	0.00106	0.00119
Figure 15c	0.001	0.00100	0.00100	0.00098	0.00100
Figure 15d	0.0001	0.00010	0.00010	0.00010	0.00010

5. Conclusions

In this work, we are dedicated to addressing the two most common and important issues involved in the MIMO compliant mechanism synthesis. One is the de facto hinge problem, which is solved by striking a good balance between structural flexibility and stiffness with the weighted objective function (8); the other is the movement coupling issue, and it is tackled through the introduction of multi-constraint conditions used to suppress both the output and input decouplings. Numerical examples show that the proposed optimization model (13) is effective in handling both problems. As a result, not only can the stress concentration (excessive local strain energy density) of the compliant mechanism be greatly alleviated, but also high-precision MIMO compliant mechanisms with fully decoupling property are obtained. In addition, only two parameters (i.e., coupling indices $[\delta]$ and $[\gamma]$) need to be set manually, whose influences on optimized results are already studied in detail. The present method is quite convenient for designing the hinge-free and completely decoupled MIMO compliant mechanisms, since it possesses the self-adaptive ability and does not need the setting of many empirical parameters. Further development can be made by replacing the traditional SIMP based topology optimization approach with new popular methods (e.g., the feature-driven method [33] and the SEMDOT algorithm [45]), in order to achieve more complicated and valuable design results with clear and smooth boundaries that could be imported into the CAD systems directly without tedious post-processing. Moreover, since the optimization design of 3D compliant mechanisms is more practical in engineering application, our future work will improve the efficiency and calculation scale of the proposed method by parallel calculation or reduced-order means, and then extend it to deal with complex 3D cases.

Author Contributions: Investigation, W.Z.; writing—original draft, W.Z.; software H.W.; editing H.W.; preparation H.W.; writing—review, S.C. and M.Z.; conceptualization, S.C.; funding acquisition, S.C. and H.W.; supervision, M.Z. All authors have read and agreed to the published version of the manuscript.

Funding: This research was funded by the National Natural Science Foundation of China (Grant No. 11702254), the Key Science and Technology Program of Henan Province (Grant No. 212102210068), the Key Scientific Research Projects of Universities in Henan Province (Grant No. 21A130003), and the Songshan Laboratory Project (Grant No. 221100211000-01).

Institutional Review Board Statement: Not applicable.

Informed Consent Statement: Not applicable.

Data Availability Statement: The data that support the findings of this study are available from the corresponding author upon reasonable request.

Conflicts of Interest: The authors declare that they have no known competing financial interest or personal relationship that could have appeared to influence the work reported in this paper.

References

1. Howell, L.L. *Compliant Mechanisms*; John Wiley & Sons: New York, NY, USA, 2001.
2. Sigmund, O. On the design of compliant mechanisms using topology optimization. *Mech. Struct. Mach.* **1997**, *25*, 493–524. [[CrossRef](#)]
3. Chen, S.K.; Wang, M.Y. Conceptual design of compliant mechanisms using level set method. *Front. Mech. Eng.* **2006**, *1*, 131–145. [[CrossRef](#)]

4. Hao, G.B.; Yu, J.J.; Li, H.Y. A brief review on nonlinear modeling methods and applications of compliant mechanisms. *Front. Mech. Eng.* **2016**, *11*, 119–128. [[CrossRef](#)]
5. Zhu, B.L.; Zhang, X.M.; Zhang, H.C.; Liang, J.W.; Zang, H.Y.; Li, H.; Wang, R.X. Design of compliant mechanisms using continuum topology optimization: A review. *Mech. Mach. Theory* **2020**, *143*, 103622. [[CrossRef](#)]
6. Her, I.; Midha, A. A Compliance number concept for compliant mechanisms, and type synthesis. *J. Mech. Des.* **1987**, *109*, 348–355. [[CrossRef](#)]
7. Howell, L.L.; Midha, A. A loop-closure theory for the analysis and synthesis of compliant mechanisms. *J. Mech. Des.* **1996**, *118*, 121–125. [[CrossRef](#)]
8. Stankiewicz, G.; Dev, C.; Steinmann, P. Geometrically nonlinear design of compliant mechanisms: Topology and shape optimization with stress and curvature constraints. *Comput. Meth. Appl. Mech. Eng.* **2022**, *397*, 115161. [[CrossRef](#)]
9. Zhu, B.L.; Wang, R.X.; Liang, J.W.; Lai, J.H.; Zhang, H.C.; Li, H.; Li, H.; Nishiwaki, S.; Zhang, X.M. Design of compliant mechanisms: An explicit topology optimization method using end-constrained spline curves with variable width. *Mech. Mach. Theory* **2022**, *171*, 104713. [[CrossRef](#)]
10. Wang, R.X.; Zhang, X.M.; Zhu, B.L.; Qu, F.H.; Chen, B.C.; Liang, J.W. Hybrid explicit–implicit topology optimization method for the integrated layout design of compliant mechanisms and actuators. *Mech. Mach. Theory* **2022**, *171*, 104750. [[CrossRef](#)]
11. Liang, K.X.; Zhu, D.C.; Liu, J. Topology optimization of a spatial compliant parallel mechanism based on constant motion transmission characteristic matrix. *Mech. Mach. Theory* **2023**, *180*, 105125. [[CrossRef](#)]
12. Emmendoerfer, H., Jr.; Maute, K.; Fancello, E.A.; Silva, E.C.N. A level set-based optimized design of multi-material compliant mechanisms considering stress constraints. *Comput. Meth. Appl. Mech. Eng.* **2022**, *391*, 114556. [[CrossRef](#)]
13. Bendsoe, M.P.; Kikuchi, N. Generating optimal topologies in structural design using a homogenization method. *Comput. Meth. Appl. Mech. Eng.* **1988**, *71*, 197–224. [[CrossRef](#)]
14. Zhou, M.; Rozvany, G.I.N. The COC algorithm, Part II: Topological, geometrical and generalized shape optimization. *Comput. Meth. Appl. Mech. Eng.* **1991**, *89*, 309–336. [[CrossRef](#)]
15. Sigmund, O. A 99 line topology optimization code written in Matlab. *Struct. Multidiscip. Optim.* **2001**, *21*, 120–127. [[CrossRef](#)]
16. Ferrari, F.; Sigmund, O. A new generation 99 line Matlab code for compliance topology optimization and its extension to 3D. *Struct. Multidiscip. Optim.* **2020**, *62*, 2211–2228. [[CrossRef](#)]
17. Wang, Y.J.; Liao, Z.Y.; Ye, M.; Zhang, Y.; Li, W.H.; Xia, Z.H. An efficient isogeometric topology optimization using multilevel mesh, MGCG and local-update strategy. *Adv. Eng. Softw.* **2020**, *139*, 102733. [[CrossRef](#)]
18. Xie, Y.M.; Steven, G.P. A simple evolutionary procedure for structural optimization. *Comput. Struct.* **1993**, *49*, 885–896. [[CrossRef](#)]
19. Huang, X.; Xie, Y.M. Convergent and mesh-independent solutions for the bi-directional evolutionary structural optimization method. *Finite Elem. Anal. Des.* **2007**, *43*, 1039–1049. [[CrossRef](#)]
20. Xia, L.; Zhang, L.; Xia, Q.; Shi, T.L. Stress-based topology optimization using bi-directional evolutionary structural optimization method. *Comput. Meth. Appl. Mech. Eng.* **2018**, *333*, 356–370. [[CrossRef](#)]
21. Xia, L.; Xia, Q.; Huang, X.D.; Xie, Y.M. Bi-directional evolutionary structural optimization on advanced structures and materials: A comprehensive review. *Arch. Comput. Method Eng.* **2018**, *25*, 437–478. [[CrossRef](#)]
22. Da, D.C.; Xia, L.; Li, G.Y.; Huang, X.D. Evolutionary topology optimization of continuum structures with smooth boundary representation. *Struct. Multidiscip. Optim.* **2018**, *57*, 2143–2159. [[CrossRef](#)]
23. Wang, H.X.; Liu, J.; Wen, G.L. An efficient evolutionary structural optimization method for multi-resolution designs. *Struct. Multidiscip. Optim.* **2020**, *62*, 787–803. [[CrossRef](#)]
24. Wang, M.Y.; Wang, X.M.; Guo, D.M. A level set method for structural topology optimization. *Comput. Meth. Appl. Mech. Eng.* **2003**, *192*, 227–246. [[CrossRef](#)]
25. Allaire, G.; De Gournay, F.; Jouve, F.; Toader, A.M. Structural optimization using topological and shape sensitivity via a level set method. *Control Cybern.* **2005**, *34*, 59–80.
26. Wei, P.; Li, Z.Y.; Li, X.P.; Wang, M.Y. An 88-line MATLAB code for the parameterized level set method based topology optimization using radial basis functions. *Struct. Multidiscip. Optim.* **2018**, *58*, 831–849. [[CrossRef](#)]
27. Cai, S.Y.; Zhang, W.H.; Zhu, J.H.; Gao, T. Stress constrained shape and topology optimization with fixed mesh: A B-spline finite cell method combined with level set function. *Comput. Meth. Appl. Mech. Eng.* **2014**, *278*, 361–387. [[CrossRef](#)]
28. Wei, P.; Wang, W.W.; Yang, Y.; Wang, M.Y. Level set band method: A combination of density-based and level set methods for the topology optimization of continuums. *Front. Mech. Eng.* **2020**, *15*, 390–405. [[CrossRef](#)]
29. Xia, Q.; Shi, T.L.; Xia, L. Stable hole nucleation in level set based topology optimization by using the material removal scheme of BESO. *Comput. Meth. Appl. Mech. Eng.* **2019**, *343*, 438–452. [[CrossRef](#)]
30. Eschenauer, H.A.; Kobelev, V.V.; Schumacher, A. Bubble method for topology and shape optimization of structures. *Struct. Optim.* **1994**, *8*, 42–51. [[CrossRef](#)]
31. Cai, S.Y.; Zhang, W.H. An adaptive bubble method for structural shape and topology optimization. *Comput. Meth. Appl. Mech. Eng.* **2020**, *360*, 112778. [[CrossRef](#)]
32. Zhou, Y.; Zhang, W.H.; Zhu, J.H.; Xu, Z. Feature-driven topology optimization method with signed distance function. *Comput. Meth. Appl. Mech. Eng.* **2016**, *310*, 1–32. [[CrossRef](#)]
33. Zhang, W.H.; Zhou, Y.; Zhu, J.H. A comprehensive study of feature definitions with solids and voids for topology optimization. *Comput. Meth. Appl. Mech. Eng.* **2017**, *325*, 289–313. [[CrossRef](#)]

34. Xu, Z.; Zhang, W.H.; Zhou, Y.; Zhu, J.H. Multiscale topology optimization using feature-driven method. *Chin. J. Aeronaut.* **2020**, *33*, 621–633. [[CrossRef](#)]
35. Guo, X.; Zhang, W.S.; Zhong, W.L. Doing topology optimization explicitly and geometrically—A new moving morphable components based framework. *J. Appl. Mech.-Trans. ASME* **2014**, *81*, 081009. [[CrossRef](#)]
36. Zhang, W.S.; Yuan, J.; Zhang, J.; Guo, X. A new topology optimization approach based on Moving Morphable Components (MMC) and the ersatz material model. *Struct. Multidiscip. Optim.* **2016**, *53*, 1243–1260. [[CrossRef](#)]
37. Bai, J.T.; Zuo, W.J. Hollow structural design in topology optimization via moving morphable component method. *Struct. Multidiscip. Optim.* **2019**, *61*, 187–205. [[CrossRef](#)]
38. Zhang, W.H.; Zhao, L.Y.; Gao, T.; Cai, S.Y. Topology optimization with closed B-splines and Boolean operations. *Comput. Meth. Appl. Mech. Eng.* **2017**, *315*, 652–670. [[CrossRef](#)]
39. Wang, X.; Long, K.; Hoang, V.N.; Hu, P. An explicit optimization model for integrated layout design of planar multi-component systems using moving morphable bars. *Comput. Meth. Appl. Mech. Eng.* **2018**, *342*, 46–70. [[CrossRef](#)]
40. Cai, S.Y.; Zhang, W.H. Stress constrained topology optimization with free-form design domains. *Comput. Meth. Appl. Mech. Eng.* **2015**, *289*, 267–290. [[CrossRef](#)]
41. Jiu, L.P.; Zhang, W.H.; Meng, L.; Zhou, Y.; Chen, L. A CAD-oriented structural topology optimization method. *Comput. Struct.* **2020**, *239*, 106324. [[CrossRef](#)]
42. Wu, Z.J.; Xia, L.; Wang, S.T.; Shi, T.L. Topology optimization of hierarchical lattice structures with substructuring. *Comput. Meth. Appl. Mech. Eng.* **2019**, *345*, 602–617. [[CrossRef](#)]
43. Long, K.; Gu, C.L.; Wang, X.; Liu, J.; Du, Y.X.; Chen, Z.; Saeed, N. A novel minimum weight formulation of topology optimization implemented with reanalysis approach. *Int. J. Numer. Methods Eng.* **2019**, *120*, 567–579. [[CrossRef](#)]
44. Wein, F.; Dunning, P.D.; Norato, J.A. A review on feature-mapping methods for structural optimization. *Struct. Multidiscip. Optim.* **2020**, *62*, 1597–1638. [[CrossRef](#)]
45. Fu, Y.F.; Rolfe, B.; Chiu, L.N.S.; Wang, Y.; Huang, X.D.; Ghabraie, K. SEMDOT: Smooth-edged material distribution for optimizing topology algorithm. *Adv. Eng. Softw.* **2020**, *150*, 102921. [[CrossRef](#)]
46. Wang, M.Y. Mechanical and geometric advantages in compliant mechanism optimization. *Front. Mech. Eng.* **2009**, *4*, 229–241. [[CrossRef](#)]
47. Zhu, B.L.; Zhang, X.M.; Fatikow, S. A multi-objective method of hinge-free compliant mechanism optimization. *Struct. Multidiscip. Optim.* **2014**, *49*, 431–440. [[CrossRef](#)]
48. Zhu, B.L.; Zhang, X.M.; Fatikow, S. Level set-based topology optimization of hinge-free compliant mechanisms using a two-step elastic modeling method. *J. Mech. Des.* **2014**, *136*, 031007. [[CrossRef](#)]
49. Da, D.C.; Chen, W. Simple strategy toward tailoring fracture properties of brittle architected materials. *Int. J. Numer. Methods Eng.* **2023**, *124*, 334–357. [[CrossRef](#)]
50. Da, D.C. Model reduction on 3D fracture resistance design. *J. Comput. Phys.* **2022**, *463*, 111274. [[CrossRef](#)]
51. Da, D.C.; Qian, X.P. Fracture resistance design through biomimicry and topology optimization. *Extrem. Mech. Lett.* **2020**, *40*, 100890. [[CrossRef](#)]
52. Yin, L.Z.; Ananthasuresh, G.K. Design of distributed compliant mechanisms. *Mech. Based Des. Struct. Mech.* **2003**, *31*, 151–179. [[CrossRef](#)]
53. Zhu, B.L.; Zhang, X.M. A new level set method for topology optimization of distributed compliant mechanisms. *Int. J. Numer. Methods Eng.* **2012**, *91*, 843–871. [[CrossRef](#)]
54. Luo, J.Z.; Luo, Z.; Chen, S.K.; Tong, L.Y.; Wang, M.Y. A new level set method for systematic design of hinge-free compliant mechanisms. *Comput. Meth. Appl. Mech. Eng.* **2008**, *198*, 318–331. [[CrossRef](#)]
55. Pereira, A.D.; Cardoso, E.L. On the influence of local and global stress constraint and filtering radius on the design of hinge-free compliant mechanisms. *Struct. Multidiscip. Optim.* **2018**, *58*, 641–655. [[CrossRef](#)]
56. Dunning, P.D. Minimum length-scale constraints for parameterized implicit function based topology optimization. *Struct. Multidiscip. Optim.* **2018**, *58*, 155–169. [[CrossRef](#)]
57. Zhan, J.J.; Luo, Y.J. Robust topology optimization of hinge-free compliant mechanisms with material uncertainties based on a non-probabilistic field model. *Front. Mech. Eng.* **2019**, *14*, 201–212. [[CrossRef](#)]
58. Zhu, B.L.; Zhang, X.M.; Wang, N.F. Topology optimization of hinge-free compliant mechanisms with multiple outputs using level set method. *Struct. Multidiscip. Optim.* **2013**, *47*, 659–672. [[CrossRef](#)]
59. Krishnakumar, A.; Suresh, K. Hinge-free compliant mechanism design via the topological level-set. *J. Mech. Des.* **2015**, *137*, 031406. [[CrossRef](#)]
60. Zhu, B.L.; Chen, Q.; Jin, M.H.; Zhang, X.M. Design of fully decoupled compliant mechanisms with multiple degrees of freedom using topology optimization. *Mech. Mach. Theory* **2018**, *126*, 413–428. [[CrossRef](#)]
61. Du, Y.S.; Li, T.M.; Jiang, Y.; Zhang, J.L. Output decoupling property of planar flexure-based compliant mechanisms with symmetric configuration. *Mech. Sci.* **2016**, *7*, 49–59. [[CrossRef](#)]
62. Wang, H.; Zhang, X.M. Input coupling analysis and optimal design of a 3-DOF compliant micro-positioning stage. *Mech. Mach. Theory* **2008**, *43*, 400–410. [[CrossRef](#)]
63. Hao, G.B.; Yu, J.J. Design, modelling and analysis of a completely-decoupled XY compliant parallel manipulator. *Mech. Mach. Theory* **2016**, *102*, 179–195. [[CrossRef](#)]

64. Zhu, W.L.; Zhu, Z.W.; Guo, P.; Ju, B.F. A novel hybrid actuation mechanism based XY nanopositioning stage with totally decoupled kinematics. *Mech. Syst. Signal Proc.* **2018**, *99*, 747–759. [[CrossRef](#)]
65. Li, Y.M.; Xu, Q.S. Design and analysis of a totally decoupled flexure-based XY parallel micromanipulator. *IEEE Trans. Robot.* **2009**, *25*, 645–657. [[CrossRef](#)]
66. Svanberg, K. The method of moving asymptotes—A new method for structural optimization. *Int. J. Numer. Methods Eng.* **1987**, *24*, 359–373. [[CrossRef](#)]

Disclaimer/Publisher’s Note: The statements, opinions and data contained in all publications are solely those of the individual author(s) and contributor(s) and not of MDPI and/or the editor(s). MDPI and/or the editor(s) disclaim responsibility for any injury to people or property resulting from any ideas, methods, instructions or products referred to in the content.